Deformation of a two-dimensional drop at non-zero Reynolds number in time-periodic extensional flows: numerical simulation

By KAUSIK SARKAR AND WILLIAM R. SCHOWALTER

Department of Chemical Engineering, University of Illinois at Urbana-Champaign, Urbana, IL 61801, USA

The shape of a two-dimensional viscous drop deforming in several time-dependent flow fields, including that due to a potential vortex, has been studied. Vortex flow was approximated by linearizing the induced velocity field at the drop centre, giving rise to an extensional flow with rotating axes of stretching. A generalization of the potential vortex, a flow we have called *rotating extensional flow*, occurs when the frequency of revolution of the flow is varied independently of the shear rate. Drops subjected to this forcing flow exhibit an interesting resonance phenomenon. Finally we have studied drop deformation in an *oscillatory extensional flow*.

Calculations were performed at small but non-zero Reynolds numbers using an ADI front-tracking/finite difference method. We investigate the effects of interfacial tension, periodicity, viscosity ratio, and Reynolds number on the drop dynamics. The simulation reveals interesting behaviour for steady stretching flows, as well as time-dependent flows. For a steady extensional flow, the drop deformation is found to be non-monotonic with time in its approach to an equilibrium value. At sufficiently high Reynolds numbers, the drop experiences multiple growth–collapse cycles, with possible axes reversal, before reaching a final shape. For a vortex flow, the long-time deformation reaches a steady value, and the drop attains a revolving steady elliptic shape. For rotating extensional flows as well as oscillatory extensional flows, the maximum value of deformation displays resonance with variation in parameters, first increasing and then decreasing with increasing interfacial tension or forcing frequency. A simple ODE model with proper forcing is offered to explain the observed phenomena.

1. Introduction

Drop deformation plays an important role in a number of natural and industrially relevant multiphase flows. In such a flow the suspended phase disperses in drops of varied sizes and shapes in the carrier phase. There is competing dynamics between the interfacial tension, favouring spherical drops, and the flow tending to deform them. The resulting drop shape affects the flow, giving rise to a two-way-coupled interaction. Therefore a basic understanding of the drop dynamics is essential for an accurate description of the rheology of the suspension. Moreover details of the flow itself are of considerable theoretical interest, for they pose a challenging nonlinear free-boundary problem, where boundary conditions are prescribed on a surface that is determined only as a part of the solution.

Since the pioneering research on viscous drop deformation by Taylor (1932, 1934, 1964), continued effort has provided major advances in our understanding of drop behaviour and its effect on bulk properties (see Stone 1994, for a review). Taylor invented the four-roll mill and successfully used it to study the deformation process. Since then the apparatus has been applied almost exclusively to create a variety of linear flows, combining stretching and rotation, that led to different deformations. The experiments have provided invaluable insights into the deformation process, and have shaped the underlying theoretical framework. Careful observations led to broad classifications (Tanner & Huilgol 1975; Tanner 1976) such as strong flows, which tend to cause large deformation, and weak flows, which do not. However the classification is based on the local gradient of the flow, and is essentially valid only for motions with constant stretch history (MCSH). Early on, the inadequacies of such a static characterization for time-dependent flows were realized (Astarita 1979), and accordingly more accurate criteria for general unsteady flows have been devised. But they remained kinematic in nature, with no input from the effects of the drop on the flow. Incorporation of the dynamics into the criteria was attempted by Olbricht, Rallison & Leal (1982), who studied evolution equations for representative micro-variables of deformation. Szeri, Wiggins & Leal (1991) introduced time-varying flow, and studied the resultant non-autonomous equation from a dynamical system point of view. The criteria emerging from their work went beyond the linear stability analysis for the initiation of stretching, and encompassed information about global dynamics. Most of these theoretical explorations were supported by experiments performed with an improved computer-controlled four-roll mill developed by Bentley & Leal (1986*a*, *b*).

A few years ago Deiber & Schowalter (1992) suggested the potential vortex as a useful base flow to study micro-rheological behaviour. In this flow a drop or a blob of polymer experiences a time-dependent non-viscometric stretching that provides an interesting point of departure from the four-roll mill or the Maxwell orthogonal rheometer. For turbulent flow of an emulsion or a polymeric solution, a potential vortex could arguably provide pertinent information not accessible through a four-roll mill. Furthermore, approximate experimental realization of a potential vortex is possible (Hopfinger, Browand & Gagne 1982; Maxworthy, Hopfinger & Redekopp 1985). To investigate the viability and usefulness of such a device we report here the results of numerical simulations of a Newtonian drop in a potential vortex and other related flows.

The small particle size, and therefore the small Reynolds number of such viscosity-dominated flows, has allowed a linearization in modelling. Most studies of drop deformation have been restricted to linearized Stokes flow. Stokes flow has been studied by semi-analytic methods at the limit of small deformation (Rallison 1984; Stone 1994), or by boundary-element methods (Pozrikidis 1992). Free surface flows have also been studied widely at the other limit, an inviscid potential flow. Although the approximation is valid, and therefore has provided useful information for inertia-driven dynamics of bubbles (Blake & Gibson 1987), the popularity of the approach is largely due to its analytical tractability. Potential flow is also dealt with by a boundary integral/element method that solves the Laplace equation. Recent years have seen other means of directly solving the full Navier–Stokes equation for problems with deformable surfaces, such as finite element or finite difference methods.

We use a front-tracking/finite difference method developed by Tryggvason and coworkers (see e.g. Unverdi & Tryggvason 1988; Esmaeeli & Tryggvason 1998, 1999). As a preliminary case study we here restrict our calculation to two dimensions.

The problem at hand does not allow any axisymmetric reduction of the full three-dimensional case. However the interesting physics that are revealed by the far less expensive two-dimensional computation would have their qualitative analogues in the actual problem, and hence the simplification is justified. Furthermore, useful guidelines are provided for future three-dimensional undertakings. The original method has been substantially enhanced with a time splitting ADI scheme allowing low Reynolds number simulation. We are restricted to non-zero Reynolds number (the lowest Reynolds number treated here is 0.1). However, our choice is dictated by the generality over boundary element methods, and computational advantages over finite difference (with a body-fitted coordinate system) or finite element implementations. Seth & Pozrikidis (1995) have investigated the effects of finite Reynolds number on two-dimensional drop deformation in a shear flow with a similar method. It is probably also pertinent to mention that recently there have been other methods similar in spirit to front-tracking, such as the level-set method, developed by Osher, Sethian and their collaborators. These have been applied with success to a number of fluid problems (Sussman & Smereka 1997). Sections 2, 3 and 4 describe the mathematical formulation of the problem and its numerical implementation. The results are presented for three different Reynolds numbers in §5. The relevant parameters are systematically varied and the effects collated and explained. In §6 we summarize our findings. A simple model capturing the essential trends of the numerical results is presented in the Appendix. In a companion paper (Sarkar & Schowalter 2001) we have undertaken an analytical study of the same phenomena which validates the numerical results, and further explains the observations.

As mentioned above, one of the primary aims of the work is to investigate vortex flow kinematics in drop deformation. However the linearized vortex model is a special case of more general rotating extensional flows, where the axes of stretching are rotating with time. We have furnished a detailed investigation of the effects of such a flow on a drop. Lastly we consider the case of an oscillatory extensional flow. All of the flows investigated here are extensional, non-vortical, and time dependent. The importance of an extensional flow in drop deformation has been noted by Taylor – a very viscous drop that would reach an equilibrium shape in a steady shear with an arbitrarily large shear rate, would extend continuously in a two-dimensional extensional flow, once the rate exceeds a critical value.

2. Vortex flow and other time-dependent flows

We elaborate here on the interesting kinematics of potential vortex flow with respect to individual fluid elements or embedded drops or polymer blobs. A fluid element in a potential vortex revolves around the origin of the vortex but experiences no rotation. As the element revolves the principal axes of the stretching rotate about the centre of the element (figure 1).

To illustrate further, we compare the flow with other possible time-periodic flows, namely widely studied oscillatory shear flow and oscillatory extensional flow (with an invariant axis of extension). In figure 2, cartoons of a drop in these three flows are shown. In potential vortex flow, the drop does not rotate, due to absence of vorticity, as it follows a periodic path around the vortex. However the flow is distinctly different from oscillatory extensional flow, where axes of extension and contraction are always along lines 1–3 and 2–4, alternatively. In the case of the vortex, the axes rotate, and hence the maximum stretching takes place at different locations along the drop interface.
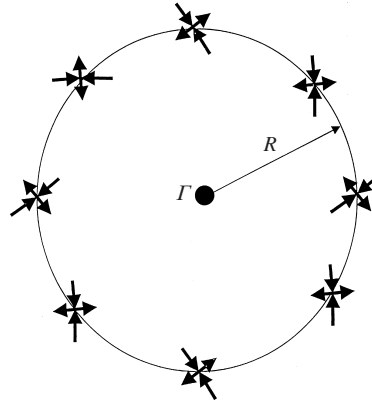
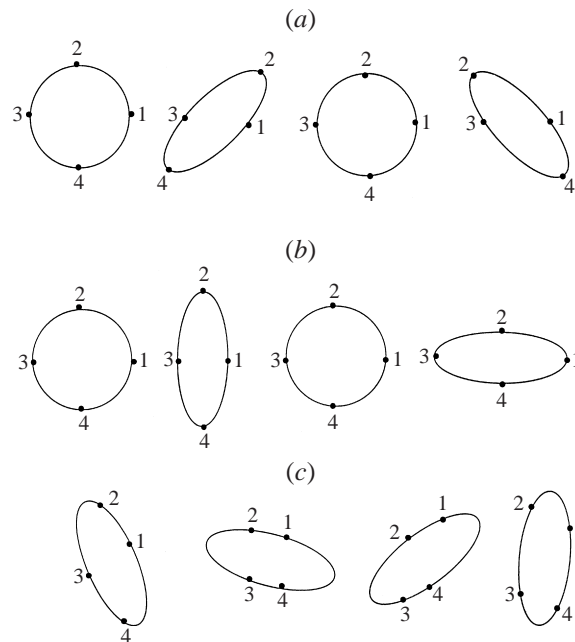FIGURE 1. Velocity gradient in a potential vortex.

FIGURE 2. Drops in different time-periodic linear flows: (*a*) oscillatory shear flow, (*b*) oscillatory extensional (OE) flow, and (*c*) vortex/generalized rotating extensional (RE) flow.

Because of the linearization approximation used in the following analysis, a drop in a vortex is, at any instant, subjected to a pure extensional flow, but the principal axes of extension rotate (figure 1). In our numerical simulation the vortex field has been represented by such a linear rotating extensional flow. The mathematical detail of the approximation is provided below. For the case of a vortex the linear approximation has a definite relationship between the shear rate of the flow and the frequency. However this linear approximation to the vortex field also indicates a more general flow field – namely a rotating extensional flow with independently varying shear rate and frequency. We have included this variant as well as the oscillatory extensional flow shown in figure 2(*b*) in our study.

3. Mathematical formulation

3.1. *Governing equations*

The velocity field $\boldsymbol{u}$ and the pressure p satisfy the equation of momentum conservation

$$\frac{\partial(\rho\boldsymbol{u})}{\partial t} + \nabla\cdot(\rho\boldsymbol{u}\boldsymbol{u}) = -\nabla p + \int_{\partial B} \mathrm{d}\boldsymbol{x}_B\,\kappa\,\boldsymbol{n}\sigma\,\delta(\boldsymbol{x}-\boldsymbol{x}_B) + \nabla\cdot\boldsymbol{\tau}, \tag{3.1}$$

in the entire domain Ω, consisting of the continuous fluid domain Ω_c and the suspended drop Ω_d with appropriate boundary conditions at an arbitrary outer boundary $\partial\Omega$. Here σ is the interfacial tension, ∂B is the surface of the drop (front) consisting of points $\boldsymbol{x}_B$, κ the local curvature, $\boldsymbol{n}$ the outward normal to the surface, and $\delta(\boldsymbol{x}-\boldsymbol{x}_B)$ is the (two-dimensional for the present problem) Dirac delta function. The deviatoric stress tensor $\boldsymbol{\tau}$ for an incompressible Newtonian fluid is given by

$$\boldsymbol{\tau} = 2\mu\boldsymbol{\varepsilon} = \mu[\nabla\boldsymbol{u} + (\nabla\boldsymbol{u})^T], \tag{3.2}$$

with μ being the viscosity, $\boldsymbol{\varepsilon}$ the strain-rate tensor, and the superscript ^{T} representing the transpose of the velocity gradient $\nabla\boldsymbol{u}$. The contribution due to the interfacial tension producing the jump in the normal stress across the interface is represented as a (singular) distributed body force, anticipating its numerical implementation to be described below. The flow field is incompressible,

$$\nabla\cdot\boldsymbol{u} = 0. \tag{3.3}$$

It is to be noted that the velocity field satisfies a single equation in both phases with a spatially varying density $\rho(\boldsymbol{x})$ that satisfies

$$\frac{\mathrm{D}\rho}{\mathrm{D}t} \equiv \frac{\partial\rho}{\partial t} + \boldsymbol{u}\cdot\nabla\rho = 0. \tag{3.4}$$

The other transport properties such as viscosity $\mu(\boldsymbol{x})$ can be similarly handled. Moreover by applying the momentum equation (3.1) in a pill-box of vanishing thickness straddling the front, one can recover traditional velocity and shear stress continuity across the front, and the jump in the normal stress due to interfacial tension (Jackson 1975, p. 36).

3.2. *Imposed flow fields*

For the vortex flow, we assume that a drop, which initially has a circular shape of radius a, is situated at a large distance R from the vortex centre (figure 1), $R \gg a$. The induced velocity field near the drop is represented by a linear approximation:

$$\boldsymbol{u}_0^{\mathrm{V}}(\boldsymbol{x}) = \boldsymbol{E}\,[\boldsymbol{x}_c(t)]\cdot\boldsymbol{x} = \boldsymbol{E}\,[R\cos\theta(t), R\sin\theta(t)]\cdot\boldsymbol{x} = \dot{\gamma}\begin{pmatrix} \sin 2\theta & -\cos 2\theta \\ -\cos 2\theta & -\sin 2\theta \end{pmatrix}\cdot\begin{pmatrix} x \\ y \end{pmatrix},$$
$$\tag{3.5}$$

where $\boldsymbol{E}\,[\boldsymbol{x}_c(t)]$ is the velocity gradient tensor evaluated at the centre of the undeformed drop $\boldsymbol{x}_c(t) = \{R\cos\theta(t), R\sin\theta(t)\}$, $\dot{\gamma} = \Gamma/(2\pi R^2)$, Γ being the circulation of the vortex. $\theta(t) = 2\pi t/T = \omega t/2$ denotes the position of the centre $\boldsymbol{x}_c$, as it revolves around the vortex with the circular speed $v_R = \Gamma/2\pi R$. The time period of revolution of the drop centre $\boldsymbol{x}_c$ is given by $T = 2\pi R/v_R = 4\pi^2 R^2/\Gamma = 2\pi/\dot{\gamma}$, and $\omega = 4\pi/T = 2\dot{\gamma}$ is the corresponding circular frequency. Note that the flow field has double the frequency of that due to the rotation around the vortex due to the symmetry at opposite points across the vortex.

The above field can be generalized to a rotational extensional flow u_0^{RE} which is given by an equation similar to (3.5) but with independent ω and $\dot{\gamma}$:

$$u_0^{\mathrm{RE}}(x) = \dot{\gamma} \begin{pmatrix} \sin \omega t & -\cos \omega t \\ -\cos \omega t & -\sin \omega t \end{pmatrix} \cdot \begin{pmatrix} x \\ y \end{pmatrix}. \qquad (3.6)$$

For $\omega = 0$, the flow reduces to a steady planar extensional flow.

Lastly, an oscillatory extensional flow is given by

$$u_0^{\mathrm{OE}} = -\dot{\gamma} \cos \omega t \begin{pmatrix} 0 & 1 \\ 1 & 0 \end{pmatrix} \cdot \begin{pmatrix} x \\ y \end{pmatrix}, \qquad (3.7)$$

Both are periodic extensional flows, (3.6) with axes rotating, and (3.7) stretching and contracting with the same frequency.

3.3. *Boundary conditions*

The kinematic condition appropriate for a material surface is imposed at the fluid/fluid boundary and determines the movement of the interface ∂B:

$$\frac{\mathrm{d}x_B}{\mathrm{d}t} = u(x_B). \qquad (3.8)$$

The velocity at a point on the interface $u(x_B)$ is related to the field velocity using the property of the delta function:

$$u(x_B) = \int_\Omega \mathrm{d}x \, \delta(x - x_B) u(x). \qquad (3.9)$$

The velocity field (3.5), (3.6) or (3.7), provides the external boundary condition at $\partial \Omega$:

$$u(x \in \partial \Omega) = u_0(x) \qquad (3.10)$$

We have already noted that the interface conditions on stress/velocity continuities are automatically met by the governing equation with spatially varying viscosities and the distributed forces (due to interfacial tension) in the field equation.

3.4. *Front-tracking preliminaries*

The drop presents an instance of multiphase flows – a suspended phase with properties (such as μ^* and ρ^* for viscosity and density) different from those (μ and ρ) in the continuous phase. The solution of such problems conventionally involves solving a governing set of equations for each phase, and matching them at the interface. The present method reduces the multiphase to a single phase with spatially varying properties, and thereby eliminates the explicit matching at the interface. For this purpose, the material properties are written as

$$\rho(x) = \rho + (\rho^* - \rho)I(x), \qquad (3.11)$$

and

$$\mu(x) = \mu + (\mu^* - \mu)I(x), \qquad (3.12)$$

where $I(x)$ is the indicator function

$$I(x) = \begin{cases} 1, & x \in \Omega_d \\ 0, & x \in \Omega_c. \end{cases} \qquad (3.13)$$

A smooth representation of the discontinuous indicator function is required for the numerical implementation of (3.11) and (3.12). Applying the gradient operator to

(3.13) we obtain

$$G(x) \equiv \nabla I(x) = n\delta^1(n \cdot (x - x_B)), \tag{3.14}$$

where δ^1 is a one-dimensional delta function. (Note that in a two-dimensional Cartesian coordinate system $\delta(x - x_B) = \delta^1(x - x_B)\delta^1(y - y_B)$). Furthermore, using the property of the delta function, we may write

$$G(x) = \int_{\partial B} \mathrm{d}x_B G(x_B)\delta^1(x - x_B)^T, \tag{3.15}$$

since $G(x)$ assumes non-zero values only on the front ∂B. The superscript ^{T} represents the tangential direction to the interface. Substituting the definition of $G(x_B)$ from (3.14), and taking the divergence, we obtain from (3.15) the following equation for $I(x)$:

$$\nabla^2 I(x) = \nabla \cdot G(x) = \int_{\partial B} \mathrm{d}x_B \nabla \cdot n\delta(x - x_B). \tag{3.16}$$

The boundary condition satisfied by $I(x)$ is $I(x \in \partial\Omega) = 0$, because the interface ∂B, in the present case, is situated far from the domain boundary $\partial\Omega$ and does not straddle it. Note that we have used the separability property of the delta function, i.e.

$$\delta(x - x_B) = \delta^1(n \cdot (x - x_B))\delta^1(x - x_B)^T. \tag{3.17}$$

Once we have numerically solved (3.16) with a smooth surrogate of the delta function (see §4 below) for $I(x)$, (3.11) and (3.12) readily furnish the desired 'smooth' fields for the properties.

4. Numerical implementation

For a finite difference implementation, the physical domain, approximated here by a large enough box (of size $L_x = L_y = 10.0$ in the unit of the drop radius) is discretized by a regular square grid. The surface of the immersed drop of radius a ($a/L_{x,y} \ll 1$) is described by line elements. Initially the elements are created by putting points on the circle. The movement of the element vertices describes the evolving shape of the drop. An adaptive regridding scheme is implemented that prevents the elements from being excessively distorted. The scheme creates/destroys elements by the insertion/removal of points on the existing front.

4.1. *Front tracking*

A smooth representation of the δ-function, needed for the numerical implementation of (3.1), (3.9), and (3.16), is provided by Peskin (1977):

$$D(x - x_B) = D^1(x - x_B)D^1(y - y_B), \tag{4.1}$$

where

$$D(x - x_B) = \frac{1}{4\Delta x}\left(1 + \cos\frac{\pi}{2\Delta x}(x - x_B)\right) \quad \text{for } |x - x_B| \leqslant 2\Delta x. \tag{4.2}$$

The representation is explicitly separable in a Cartesian coordinate system and has the desirable unit measure property (i.e. upon integration over a domain containing x_B, it results in unity). The approximation of the delta function is coupled with the discretization of the computational domain: as the discretization length Δx approaches zero, the approximant approaches infinity, as required of a family of regular functions approaching a delta function (Stakgold 1979, p. 110).

Upon substitution of the above representation of the smoothed delta function and discretization, generic integrals take the following forms:

$$\int_{\Omega} dx\, f(x)\,\delta(x - x_B) \simeq \sum_{i} \Delta x \Delta y\, f(x_i)\, D(x_i - x_B), \tag{4.3}$$

where i sums over all grid points in the domain, and

$$\int_{\partial B} dx_B\, f(x)\delta(x - x_B) \simeq \sum_{j} \Delta l_j f(x_j)\, D(x_j - x_B). \tag{4.4}$$

Here the index j sums over all front elements, and Δl_j represents the length of the jth element on the front. Expressions similar to (4.3) are used for (3.9), and those like (4.4) are used for the interfacial tension term in (3.1), and in the right-hand side of (3.16). Such representations allow a back-and-forth coupling between the discretized front and the domain variables around it. Broadly speaking we have replaced the sharp interface separating the phases by a region of sharp variation in properties, which has a finite thickness, approximately $4\Delta x$.

4.2. *Finite difference*

This formulation leaves us with a system of partial differential equations with smooth spatially varying coefficients. The front has been decoupled from the underlying flow equation, and has been retained only as a means for computing the properties at successive time steps. Note that one may choose any suitable method for the system of equations in the computational domain. We use an MAC type operator splitting/projection finite difference method. The original method solves the system in following two explicit steps. The predictor consists of finding the intermediate velocity u^* by

$$\frac{\rho^{n+1} u^* - (\rho u)^n}{\Delta t} = -\nabla \cdot (\rho u u)^n + F^n + \nabla \cdot \tau^n. \tag{4.5}$$

where F^n is the body force, which includes in the present case the contribution due to the interfacial tension. The density $\rho^{n+1}(x)$ is evaluated by (3.11) from the new front position attained by moving it explicitly with the velocity u^n. The spatial derivatives are approximated by central differences in their conservative form. The corrector step gives the final velocity at the next time step u^{n+1},

$$\frac{u^{n+1} - u^*}{\Delta t} = -\frac{1}{\rho^{n+1}} \nabla p^{n+1}. \tag{4.6}$$

Taking the divergence of (4.6), and demanding that u^{n+1} satisfies continuity, we obtain the following Poisson's equation for the pressure:

$$\nabla \cdot \left(\frac{1}{\rho^{n+1}} \nabla p^{n+1} \right) = \frac{1}{\Delta t} \nabla \cdot u^*. \tag{4.7}$$

A detailed description of the method can be found in Peyrot & Taylor (1986, p. 160). We use a staggered grid; the boundary values for the nodes just outside the computational domain are obtained by second-order interpolation. A zero Neumann condition for pressure, as has been shown to be valid for this explicit method (Easton 1972), is imposed at the boundary. Note that the final velocity field u^{n+1} is solenoidal while the intermediate velocity u^* is not.

The above explicit scheme suffers from dual restrictions on time steps – from diffusion at low Reynolds number ($\Delta t < 0.25(\Delta x)^2/v$), and from advection at high Reynolds number ($\Delta t < 2.0v/U_{max}^2$) (see Peyrot & Taylor 1986, p. 148). For our particular applications relevant to emulsions, low Reynolds number cases are important. As mentioned before, the available literature on emulsions is largely restricted to zero Reynolds number cases, and we would like to compare our results with them. To relieve the low Reynolds number restriction on time-step, we split the predictor step further, and treat the diffusive terms by ADI. A similar treatment was first successfully executed by Goda (1979) for cavity flows. The equation (4.5) for this step is split into three parts,

$$\frac{\rho^{n+1}\boldsymbol{u}^{***} - (\rho\boldsymbol{u})^n}{\Delta t} = -\nabla\cdot(\rho\boldsymbol{u}\boldsymbol{u})^n + F^n + D_{xy}(\boldsymbol{u}^n), \tag{4.8}$$

$$\rho^{n+1}\frac{\boldsymbol{u}^{**} - \boldsymbol{u}^{***}}{\Delta t} = D_{yy}(\boldsymbol{u}^{**}), \tag{4.9}$$

$$\rho^{n+1}\frac{\boldsymbol{u}^* - \boldsymbol{u}^{**}}{\Delta t} = D_{xx}(\boldsymbol{u}^*). \tag{4.10}$$

Here the viscous term in (4.5) is expressed in three parts,

$$\nabla\cdot\tau = D_{xy} + D_{yy} + D_{xx}. \tag{4.11}$$

where D_{xx} and D_{yy} are terms involving double derivatives with respect to either x or y, and D_{xy} are the mixed derivatives. While the mixed derivatives are treated along with advection in an explicit manner (4.8), the terms that involve double derivatives are handled implicitly along alternating directions, first y (4.9), and then x (4.10). We note that all the terms are retained in their conservative form in contrast to the treatment by Seth & Pozrikidis (1995). Each of these implicit equations gives rise to a tri-diagonal system that is solved by Thom's algorithm. However, while an explicit scheme does not require boundary values for the intermediate variables (those with asterisks), they need to be prescribed in an implicit method. We use

$$\boldsymbol{u}^* = \boldsymbol{u}^{**} = \boldsymbol{u}^{***} = \boldsymbol{u}^{n+1} \quad \text{at} \quad \partial\Omega, \tag{4.12}$$

and consequently the zero Neumann condition on the pressure is retained. It should be noted that some early theoretical studies by Temam indicated that imposing final step values on the intermediate variables at the boundary is a sufficient condition for convergence as $\Delta x, \Delta t \to 0$ (Peyrot & Taylor 1986, p. 165). There have been several attempts to improve the order of the method by contriving smart conditions for the intermediate velocities and the pressure (Kim & Moin 1985; Karniadakis, Israeli & Orszag 1991). However, recently Perot (1993) has shown that the present prescription is consistent with an LU decomposition of the original operator. It seems to suffice for our simulation.

Even though ADI formally removes the restriction on time steps, it is well known that in practice care is required when implementing such a fractional step algorithm. We also adhere to a CFL criterion $\Delta t < \Delta x/U_{max}$. Furthermore, the maximum norm of the velocity field is monitored for any unsatisfactory behaviour, and the time step is halved when warranted. An explicit Euler integration scheme has been used for time marching. A multigrid method (Ferziger & Peric 1996, p. 106) is applied for the solution of the Poisson equations for the pressure (4.7) and the indicator function (3.16).

5. Results

We non-dimensionalize the problem, using drop radius a and $\dot{\gamma}^{-1}$ as the length and the time scales, respectively. For the steady problem there are four non-dimensional parameters: $Re = \rho\dot{\gamma}a^2/\mu$, $k = Ca^{-1} = \sigma/(\dot{\gamma}\mu a)$, $\lambda = \mu^*/\mu$, and $\lambda_\rho = \rho^*/\rho$. For the case of a vortex the non-dimensional frequency (Strouhal number) $St = \omega/\dot{\gamma} = 2$. However for general rotational or oscillatory extensional flows the non-dimensional frequency assumes arbitrary values and signifies the effect of the periodicity. In the following we drop the prime and refer only to the non-dimensional variables. Because we have not considered gravity effects in our simulation, λ_ρ appears in the problem only through the drop Reynolds number $Re^* = Re\lambda_\rho/\lambda$. For brevity, we restrict results to the case of $\lambda_\rho = \lambda = 1.0$. Typical values for a drop of alcohol insoluble in water are $\mu^* = 0.018\,\mathrm{g\,cm^{-1}\,s^{-1}}$, $\rho^* = 0.82\,\mathrm{gm\,cm^{-3}}$ and σ, 1–$10\,\mathrm{dynes\,cm^{-1}}$ (Davies & Rideal 1963, p. 17). For such a drop of radius $a = 1\,\mathrm{cm}$ suspended in water ($\mu = 0.01\,\mathrm{g\,cm^{-1}\,s^{-1}}$, $\rho = 1.0\,\mathrm{gm\,cm^{-3}}$) and $\dot{\gamma} = 0.1\,\mathrm{s^{-1}}$, one obtains $Re = 10$, $\lambda = 1.8$, $\lambda_\rho = 0.82$ and k, 1000–$10\,000$.

In the following we have studied drop deformation with the criterion originally suggested by Taylor (1932, 1934), namely $D = (L - l)/(L + l)$, where L (l) is the maximum (minimum) distance of the drop surface from the centre. The criterion is based on the experimental observation and asymptotic result that the drop takes on an approximately elliptical shape in steady shear and extensional flows. However, for an arbitrary deformation this criterion based on the distance between pairs of only two surface points is extremely sensitive to the numerical description of the surface. In figure 3 we compare the evolution of D at different resolutions for a drop in a vortex with $k = 7.599$ and $Re = 0.1$. We note that drop shapes at any time instant (figure 3a) are almost identical for different resolutions, and yet figure 3(b) shows significantly different values of D. The present method, based on an interface smoothed over $4\Delta x$, is inherently approximate for the exact location of the interface. The rate of convergence for the long-time value of D is plotted in the inset of figure 3(b). Note that according to Tryggvason et al. (1998) even though the difference scheme is second order, the convergence rate is expected to be lower than quadratic due to smearing of the interface. In the results presented here an 81×81 grid was used. Our choice (16 grid points across the drop diameter) is based on the ability to describe the shape rather than D. The effect of domain size was also investigated by increasing it to twice the present size ($L_x = L_y = 10.0$) with no significant change in results. From our convergence study and the satisfactory match with analytical results (Sarkar & Schowalter 2001), we believe that the values of D computed below depict correct trends.

5.1. *Vortex*

As mentioned earlier, the literature on emulsions is largely restricted to steady Stokes flow. Our code is limited to low but finite Reynolds number. As a low Reynolds number case that could be fruitfully compared with Stokes flow, we choose $Re = 0.1$. Figure 4 shows the evolution of deformation D (defined above) with time for different interfacial tensions. For $k = 2.533$, the drop experiences a very large growth and

---

FIGURE 3. Convergence with increased resolution: drop deformation in a potential vortex at $Re = 0.1$ and $k = 7.599$. (a) The drop shapes at a time instant $t = 25.19$. (b) Deformation with time. Inset shows the error in D at a particular instant with resolution N, where N is the number of grid points along one of the coordinate directions. The error is computed with reference to the value of D at a 193×193 grid.
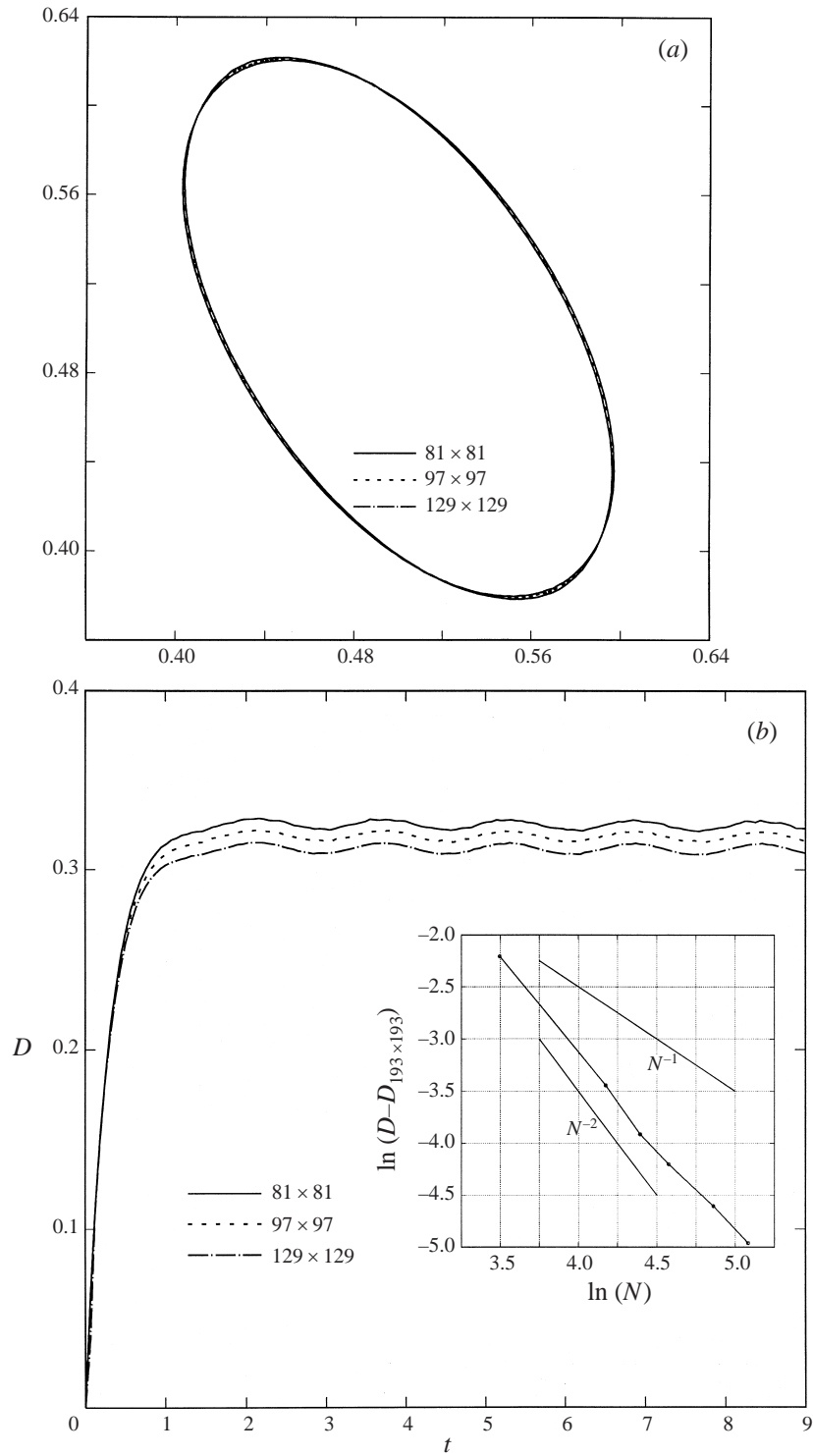
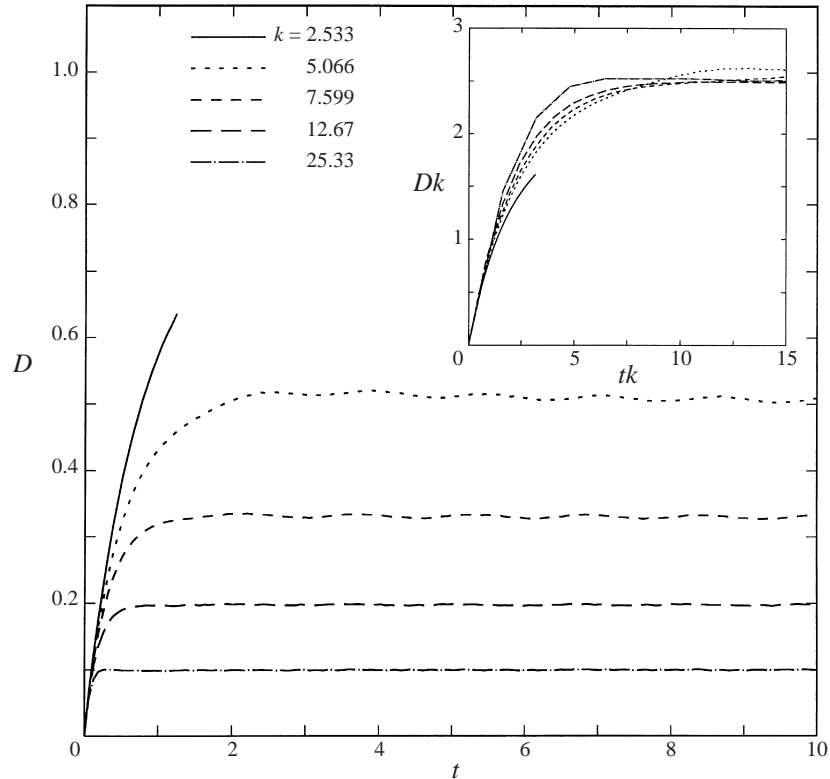FIGURE 3. For caption see facing page.

FIGURE 4. Effect of interfacial tension on drop deformation in a potential vortex at $Re = 0.1$.
Inset shows the same in scaled variables.

quickly reaches the box boundary. However as k increases, deformation is inhibited due to increased interfacial tension, and the drop remains bounded, as is evident for $k = 5.066$, 7.599, 12.67 and 25.33. The curves are similar to those obtained for a steady Stokes flow. For the latter it was shown by a perturbative analysis (Cox 1969) that in the limit of small deformation (of the order $\epsilon = k^{-1}$), $Dk \sim 1 - \exp(-tk)$. The accompanying analytical work (Sarkar & Schowalter 2001), as well as the simple ODE model in the Appendix (A 4) show the same. In the inset, D, accordingly scaled by k, plotted against tk shows an approximate collapse onto one curve for different k, except for the two lowest values of k. However it should be noted that the presence of inertia and rotation destroys the exact time dependence with tk, as has indeed been demonstrated by the simple model in the Appendix (A 5) as well as the first-order Stokes analysis (Sarkar & Schowalter 2001). The apparent collapse onto a single curve for different k is a result of the asymptotic limit of $D \sim k^{-1}$ for large k (the value $kD_\infty \sim 2.5$ is considerably higher than the first-order Stokes flow result). At large times, D reaches an almost constant value, as though an elliptic shape is rotating in response to the rotating stretching field of the vortex. However we note that the drop does not undergo rigid rotation: its deformation merely appears so.

In figure 5, we present the evolution of D with time for an intermediate Reynolds number $Re = 1.0$. Here too we observe that increased interfacial tension leads to a bounded growth. The solid and the dotted curves for $k = 2.533$ and 7.599 show unbounded growth. It should be noted that for $Re = 0.1$ (figure 4) and $k = 7.599$, the
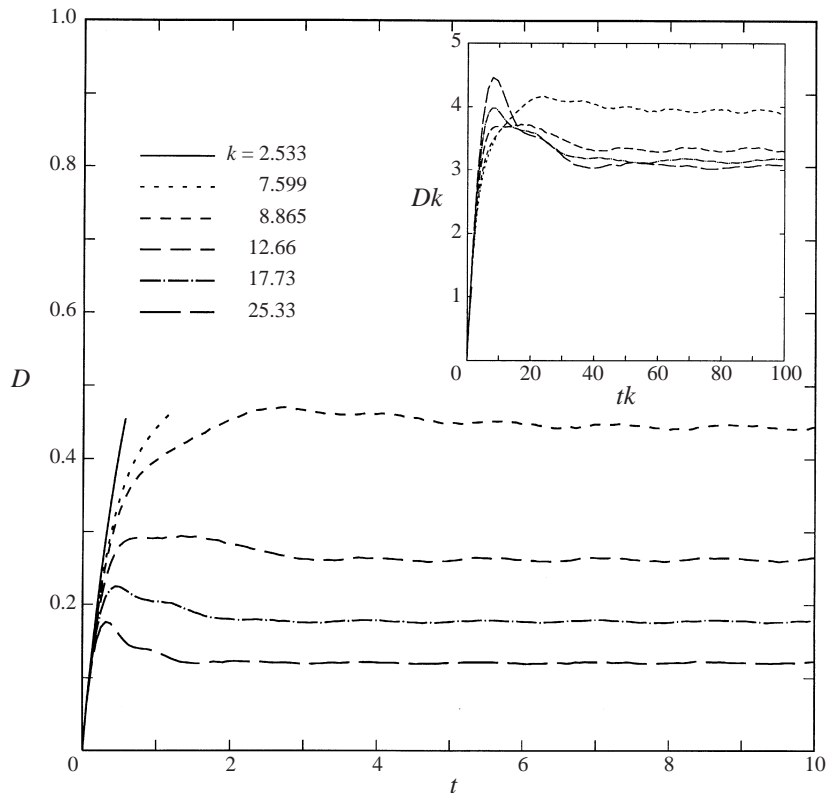
FIGURE 5. Effect of interfacial tension on drop deformation in a potential vortex at $Re = 1.0$.
Inset shows the same in scaled variables.

interfacial tension effectively inhibits the deformation at $D \simeq 0.3$. As expected, higher inertia leads to higher deformation. For $k = 8.865$, the drop shape reaches a bounded shape and with increasing interfacial tension, the steady state D decreases as k is increased. In the inset the evolution of Dk does not show as good a collapse as for $Re = 0.1$. However, as is predicted in the Appendix the long-time Dk reaches ~ 3.1 for large k. The initial overshoot in D is an effect of the increased Reynolds number of the simulation. The overshoot is even more prominent in figure 6 for $Re = 10.0$. The drop shapes (rotating counter-clockwise) plotted at early times (note that their position does not correspond to the time axis) show that the drop experiences large deformation initially, but settles down to lower values at later times. Again the scaled variable Dk exhibits a long-time limit (~ 8) independent of k. As has been shown in the Appendix this is a result true for all Re; for higher Re, $D \sim k^{-1}$ scaling occurs for larger values of k. As is evident from the above there is a critical k, below which the interfacial tension is not sufficient to inhibit the growth of deformation. Previous investigators (see Stone 1994) have analytically determined k_{crit} for steady Stokes flow. Figure 7 shows the effect of Re on k_{crit} from our simulations for the vortex. As can be expected with increased Re, k_{crit} increases sharply, indicating that higher interfacial tension is needed to balance the inertia. Note that the present case is different from the steady cases studied before, as the revolution due to the vortex also acts against the growth of the drop, and therefore k_{crit} for a given Re is lower than for a steady
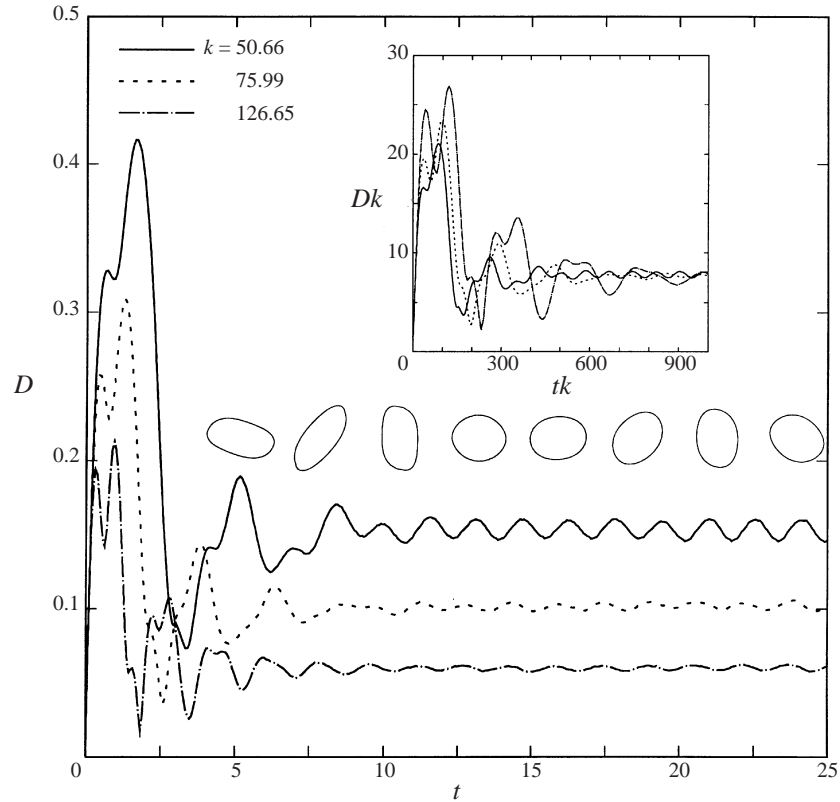
FIGURE 6. Effect of interfacial tension on drop deformation in a potential vortex at $Re = 10.0$. Inset shows the same in scaled variables. Drop shapes for $k = 50.66$ at $t = 0.69$, 1.51, 2.27, 3.13, 3.85, 4.67, 5.42 and 6.24 (from left to right), during the initial transient. The shape positions in the figure do not correspond to the time axis.

flow. Increased viscosity ratio was found to reduce deformation, as is expected from the steady Stokes flow analysis. Those results are not shown in the interest of brevity.

5.2. Rotating extensional (RE) flow

For the vortex the undisturbed flow is given by (3.5), with non-dimensional frequency $St = 2$. However, in principle one could vary St independently. As a thought experiment one could imagine a circular bath filled with a ferromagnetic fluid. Applying opposite magnetic fields along a line through the centre (i.e. putting magnets of the same polarity at opposite sides of the bath), one could set up a flow where the fluid would be rotating in four cells due to mass conservation. Along two orthogonal axes of the bath, flow would be towards and away from the centre, respectively, creating a saddle point in the middle. A drop of a second ordinary fluid suspended at the center is, therefore, in an extensional flow with shear rate $\dot{\gamma}$, determined by the strength of the applied magnetic fields. On rotating the magnetic field around the bath with a frequency ω, the desired 'rotating extensional flow' is obtained in the vicinity of the drop. Here we investigate such a general rotational extensional flow (3.6).
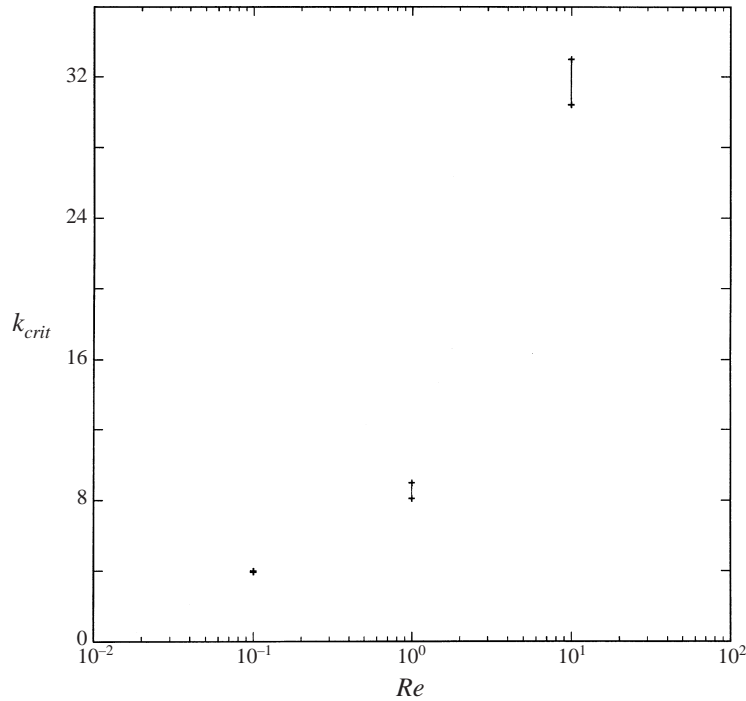
FIGURE 7. Effect of Reynolds number on the critical value of k in a potential vortex. The upper and the lower bounds indicate the closest values of k for which a bounded and an unbounded shape, respectively, are numerically found at that Re.

5.2.1. $Re = 0.1$

We first performed the limiting case of a steady stretching flow, $St = 0$, with results shown in figure 8. It is seen, as is expected, that for a low interfacial tension, $k = 5$, the drop continues an unbounded deformation, but for sufficiently high tensions it attains an equilibrium shape. In the inset we compare with the Stokes flow results of Buckmaster & Flaherty (1973). Note that their large-deformation analysis is different from our perturbative study in Sarkar & Schowalter (2001). They have provided an approximate (their equation (3.6)) as well as a numerical solution that match very well with each other (their figures 2 and 3). Here we have used the former for convenience. Note that the variable B defined in Buckmaster & Flaherty (1973) corresponds to the deformation. One can find the capillary number inverse k used here from the quantity defined by their equation (3.6) and constant area constraint of the elliptic drop. Comparison is satisfactory with enhanced deformation for finite Reynolds number numerical results. As was noted by Buckmaster & Flaherty, two branches of a non-unique curve meet at a value of $k^{-1} = 0.18$ (their scaled variable $\Omega = 4\pi\sqrt{\pi}k^{-1} \sim 4.0$). They commented that here the drop dynamics changes character with the shape displaying a flattened centre. They suggested possible onset of unsteady flow around this point. Here we find that below $k = 10$, the drop tends to stretch indefinitely.

For the case of $k = 8$, we introduce the effect of the rotation of the stretching axes by increasing St from zero. In figure 9, D is plotted as a function of time. It is seen that the deformation decreases with increasing frequency. This can be explained by the fact that due to the time dependence of the imposed flow, the point along the drop surface that experiences maximum extensional rate changes with time. Therefore
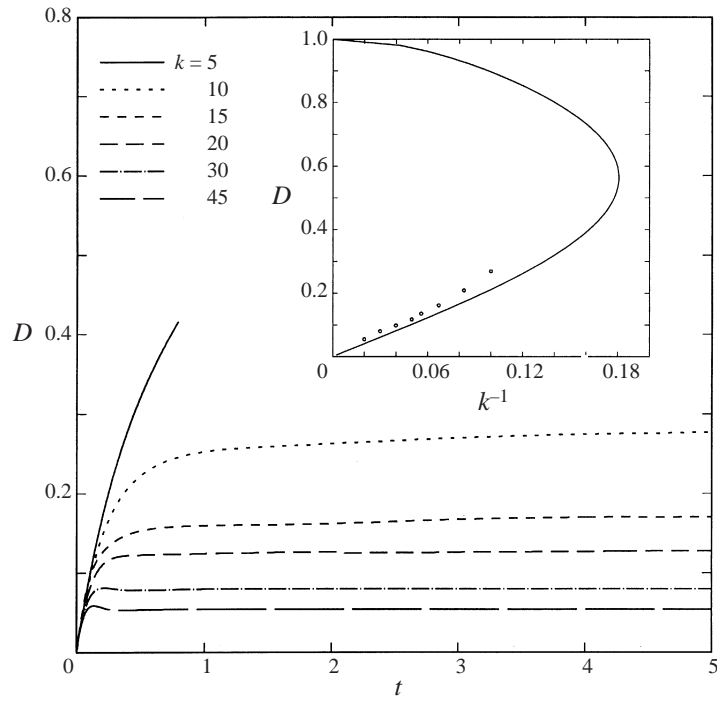
FIGURE 8. Effect of interfacial tension on drop deformation in a steady extensional (RE with $St = 0$) flow at $Re = 0.1$. In the inset we show comparison with the analytical Stokes flow results from Buckmaster & Flaherty (1973) for the long-time drop response.
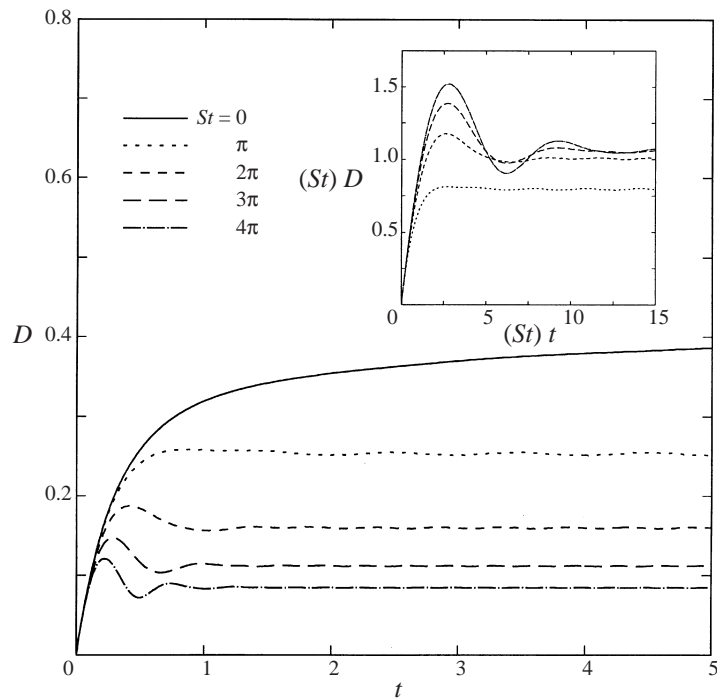
FIGURE 9. Effect of frequency on drop deformation in an RE flow at $Re = 0.1$ and $k = 8.0$. Inset shows the same in scaled variables.
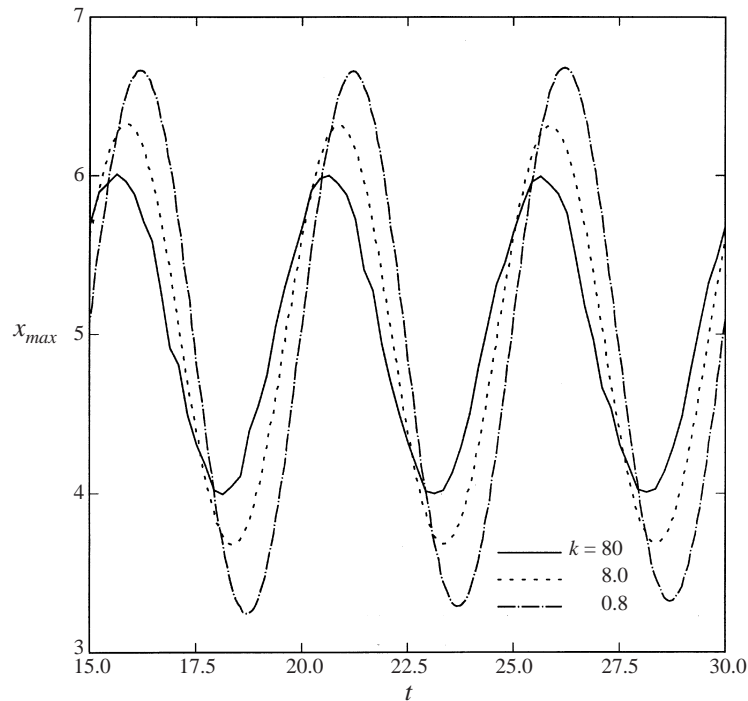
FIGURE 10. Effect of interfacial tension on the phase lag of the drop response in an RE flow at $Re = 0.1$ and $St = 0.8\pi$.

there is insufficient time to grow as much as in the steady case, the effect increasing with increasing frequency. Similar to the case in a vortex, D attains an equilibrium value, which is lower for higher frequency, after initial transient behaviour. Therefore evolution of drop shape also appears to be close to a rotating ellipse as for the vortex flow. It is shown in the Appendix that for large St long-time $D \sim St^{-1}$. StD (except for $St = 0$) is plotted in the inset against $(St)t$, and it reaches a constant value $StD \sim 1.06$ for high St. Note that in the rescaled time the maximum for different curves coincides, indicating that the transient behaviour is dominated by the unsteady term.

In figure 10, we plot the x-coordinate of the point that is the maximum distance (i.e. L) away from the drop centre (5.0, 5.0), after decay of the initial transient. For a purely periodic rotation of a rigid ellipse, the curve would execute sinusoidal motion, and would provide the phase information of the drop response. Curves are plotted for $St = 0.8\pi$, and varying interfacial tension. The drop response amplitude shows the expected decrease with increasing interfacial tension. Moreover it also displays a difference in phase lag, the interfacial tension acting as a spring component in the damped system of the viscous flow. Hence its change gives rise to a change in phase lag, as is characteristic of such systems.

In figure 11, we plot D for varying interfacial tension, at a fixed frequency $St = 4\pi$. We find that with increasing interfacial tension, D reaches its steady value more quickly. For lower interfacial tension the drop deformation oscillates with the forcing flow. For the case of $k = 1.0$ the oscillation can readily be seen to correspond to the forcing frequency (20 peaks in 20 periods). On closer scrutiny, the long-time
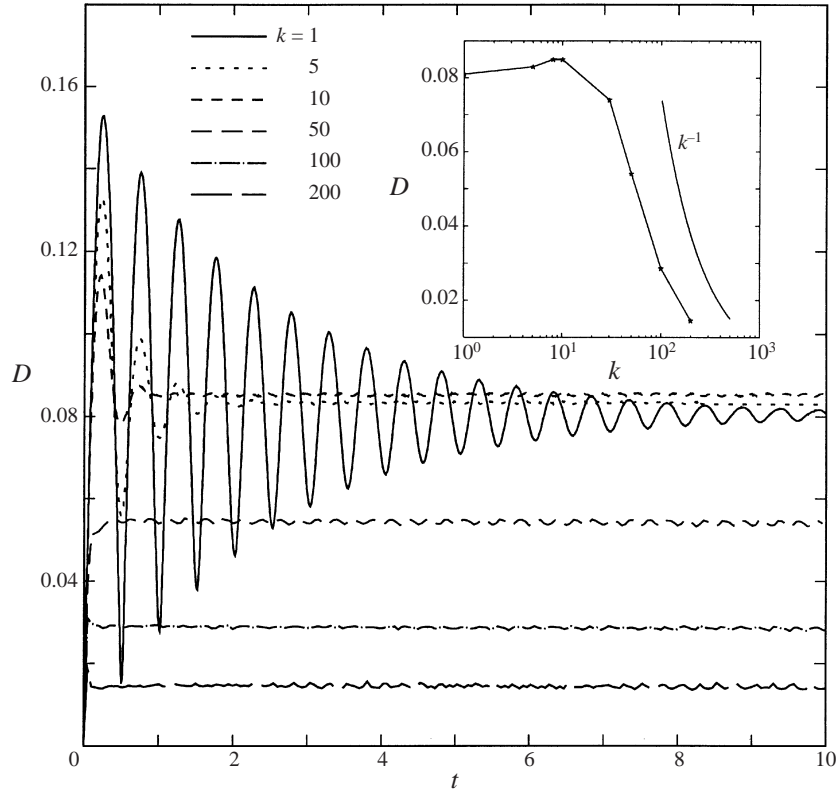
FIGURE 11. Effect of interfacial tension on drop deformation in an RE flow at $Re = 0.1$ and $St = 4\pi$. Inset shows long-time drop response for varying tension.

response reveals a surprising behaviour. D first increases with interfacial tension ($k = 1, 5, 10$), before its final decrease ($k = 50, 100, 200$). We plot the asymptotic values of D in the inset as a function of k. Here the rising portion is difficult to distinguish. We encountered this characteristic *non-monotonicity* repeatedly throughout our investigation. The decay of D as k^{-1} is also evident for large k.

In figure 12, we reinvestigate the effects of increasing frequency as in figure 9, but with a higher interfacial tension, $k = 45$. For steady stretching, the drop reaches an equilibrium shape due to the large interfacial force. As we increase the frequency, the long-time steady value of D increases up to $St = 6\pi$ and then decreases. The emerging scenario of long-time D as a function of changing frequency shown in the inset shows the narrow nature of the peak. The St^{-1} decay of D for larger frequencies is also shown.

The non-monotonicity of the curves in figures 11 and 12 is the effect of resonance in the forced damped oscillator system underlying the flow. In the Appendix such a model oscillator with proper forcing terms is constructed to explain the behaviour. Here the interfacial tension acts as a spring, viscosity as a damper, and the imposed periodic flow as the forcing. Unlike Stokes flow, owing to the finite Reynolds number, the present case also has a true mass. So the system has a *natural frequency* which increases with interfacial tension, i.e k. For a fixed forcing frequency, as in figure 11, the response peaks when the natural frequency is close to the forcing frequency. A similar resonance occurs in figure 12, where the forcing
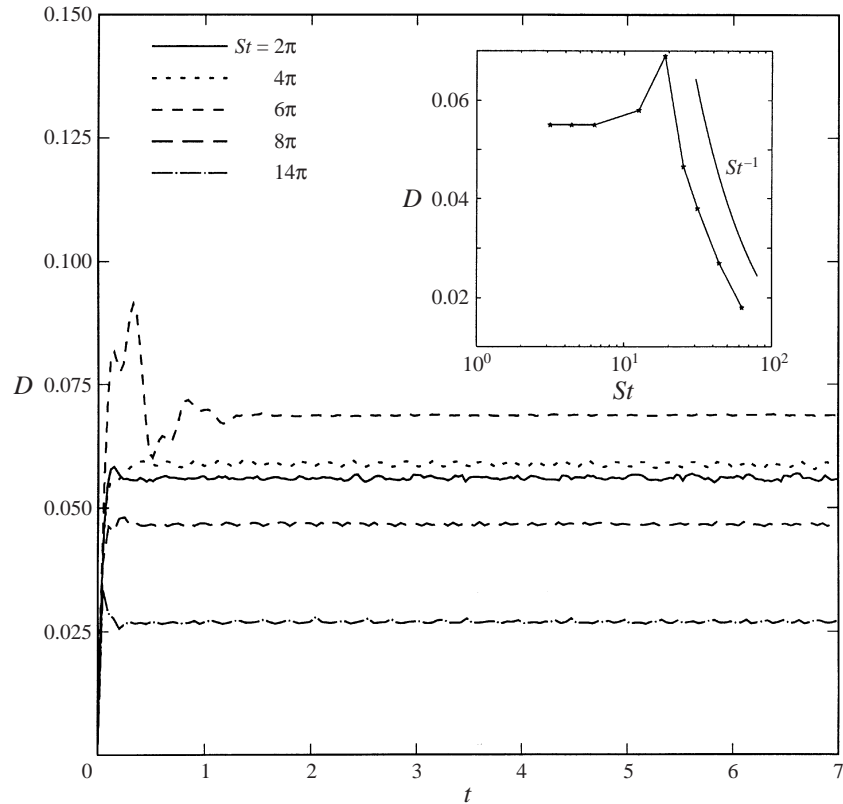
FIGURE 12. Effect of frequency on drop deformation in an RE flow at $Re = 0.1$ and $k = 45.0$. Inset shows long-time drop response for varying frequency.

frequency is varied, and the natural frequency is kept constant. The resonance was not seen for the lower value of interfacial tension in figure 9 because in the limit of zero frequency the spring force is not sufficient to balance the force due to the flow and result in an equilibrium. Therefore the initial ascending branch is absent. Similarly for the vortex with $St = 2$, the frequency is too low; there for small interfacial tension the drop experiences unbounded growth, and increasing interfacial tension leads to a monotonic decrease in the deformation. An approximate analytical solution is presented in Sarkar & Schowalter (2001) where the unsteady term of the Navier–Stokes equation is retained that dominates the convective term for large St. The results from this unsteady Stokes solution are in excellent agreement with the present numerical results. There it was also shown that resonance is absent in the Stokes solution. This substantiates our analogue to a damped mass–spring system.

5.2.2. $Re = 1.0$

We first study the deformation for a steady stretching flow (figure 13), for here the finite Reynolds number effect is evident even for a steady case. At the lowest interfacial tension value $k = 8$, one observes sharp unbounded deformation. With increasing interfacial tension, $k = 10$, 15 and 20, D reaches a steady value. However there is an inertial overshoot in D before reaching the lower long-time equilibrium
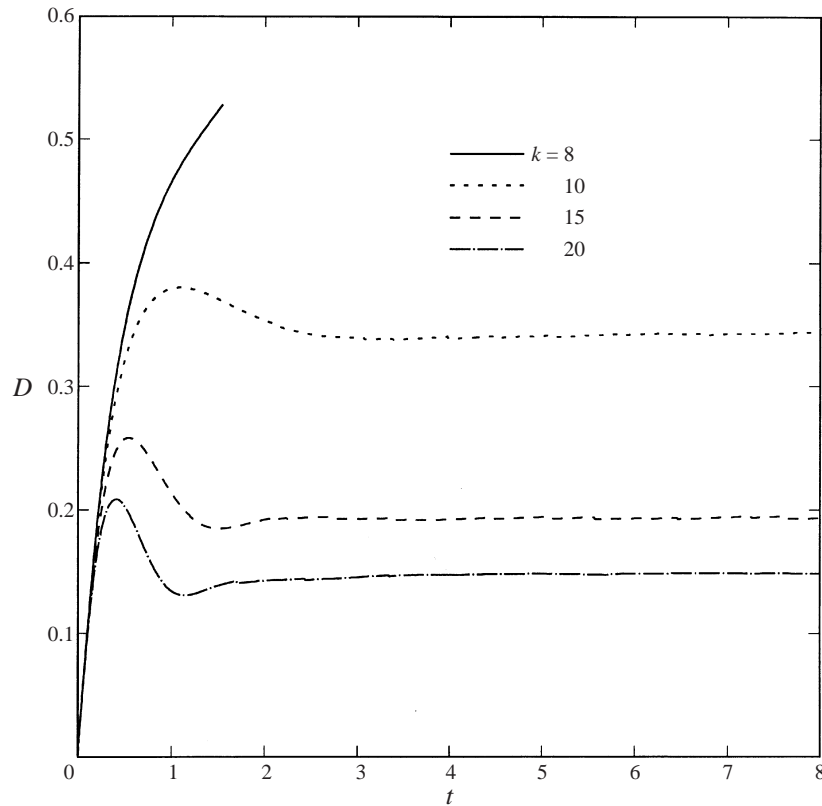
FIGURE 13. Effect of interfacial tension on drop deformation in a steady extensional
(RE with $St = 0$) flow at $Re = 1.0$.

value. In a steady Stokes flow, the drop would reach the equilibrium shape in a
monotonic way. There the forces acting on the drop are always in equilibrium, giving
rise to zero acceleration and eliminating any possibility of overshoot. Increasing the
frequency from the steady case for $k = 8$ (top curve in figure 13) shows effects (figure
not shown) similar to $Re = 0.1$ (figure 9), in that the deformation becomes bounded,
and attains lower long-time values with increasing frequency.

At $k = 20$ the time evolution of D shows non-monotonicity (figure 14) with
increasing St. Note that in the initial transient period close to the start-up, shown
in the inset, there is a crossing of the evolution curves. It is as though the evolution
starts out in accordance with our expectation – increased frequency leads to decreased
deformation – but then changes character leading to a crossover around $t = 0.6$. The
long-time D values for fixed frequency and fixed interfacial tension are plotted in
figure 15. The long-time D versus frequency has been plotted for $k = 20$ and 200.
For the smaller k, the resonance structure occurs at a lower St ($St \sim 6$) whereas for
the larger k, it is near $St = 20$. The shift in natural frequency is due to the change
in the spring component of the system caused by variation of interfacial tension.
For $St = 4\pi$, the time evolution of D for various k again reaches long-time constant
values that are plotted. They increase with increasing interfacial tension until $k = 70$,
and then sharply decrease. All the curves show the typical inverse decay with k and
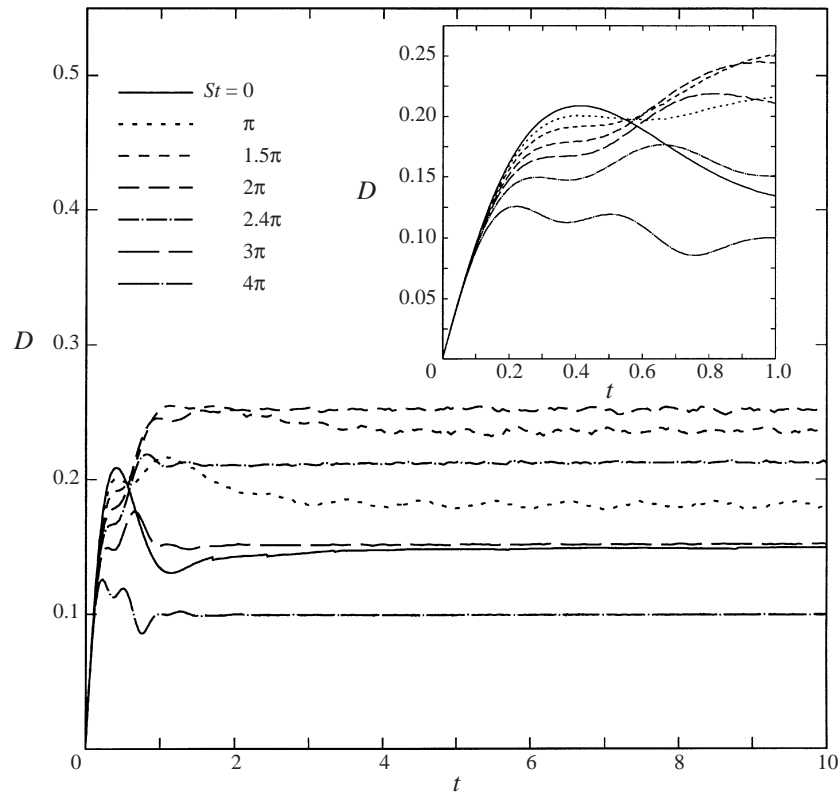St for large values.

FIGURE 14. Effect of frequency on drop deformation in an RE flow at $Re = 1.0$ and $k = 20$. Inset shows a magnification at small times.

5.2.3. $Re = 10.0$

For $Re = 10.0$, we first investigate D for a steady stretching flow in figure 16. For lower interfacial tension ($k = 8$, 16 and 30), the deformation quickly grows and the drop reaches the domain boundary. However for $k = 40$, 50, 80 and 200 meaningful shapes are obtained in the long-time limit. Here oscillations in D are more pronounced than in the lower Reynolds number cases. For $k = 80$ and 200, D reaches zero before it attains its equilibrium value. We show this phenomenon in more detail in the inset, where the maximum (L) and the minimum (l) dimensions of the drop for $k = 80$ are shown. In essence the drop experiences multiple growth–collapse cycles before reaching an equilibrium shape. Similar growth–collapse cycles are observed in the inertia-dominated oscillation of a pressurized bubble (Blake & Gibson 1987). The drop shapes at various times (corresponding approximately to the time axis) show that the drop 'snaps back' to such an extent that the major axis is orthogonal to the applied strain rate at $t = 1.32$ (the second drop trace from the left) during the second cycle. However it reverts back to being along the extension axis in the third cycle and remains so in the fourth cycle and afterward.

The time-periodic simulation with non-zero St, for $Re = 10.0$ proves computationally intensive, because of small time steps and slower disappearance of transients. For a fixed value of $k = 200$, a simulation is performed for varying forcing frequency (figure 17). D increases with increasing frequency $St = \pi$, 2π and 3π, and executes large oscillations over the full length of computation ($t = 30$). At still higher forcing
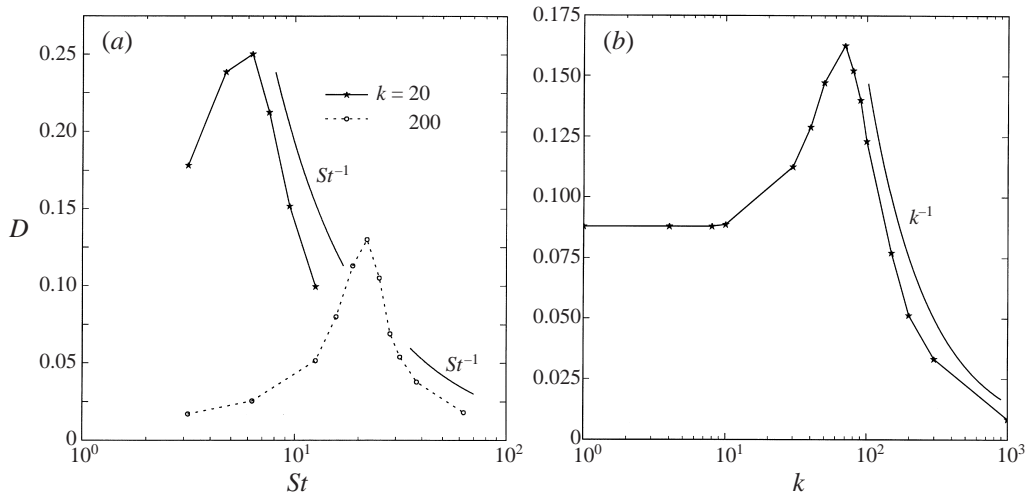
FIGURE 15. Long-time drop response in an RE flow at $Re = 1.0$ with varying (*a*) frequency; (*b*) interfacial tension, $St = 4\pi$.
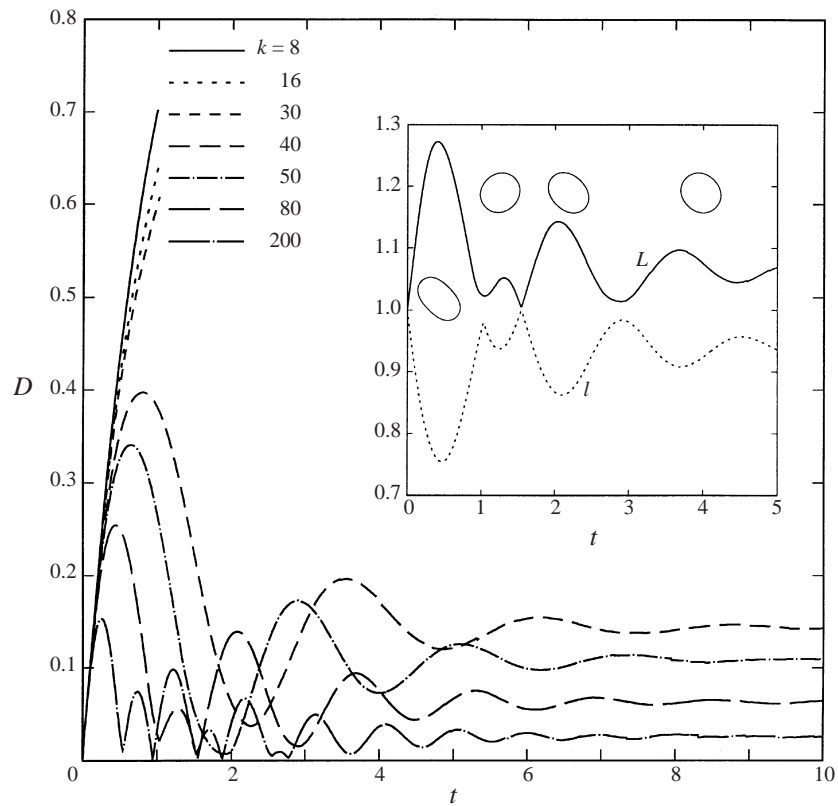

FIGURE 16. Effect of interfacial tension on drop deformation in a steady extensional (RE with $St = 0$) flow at $Re = 10.0$. Inset shows evolution of maximum (solid) and minimum (dotted) distances of the drop interface from its centre for $k = 80$. Also the drop shapes at $t = 0.5, 1.32, 2.04$ and 4.09 are shown. Their positions approximately correspond to the time axis.
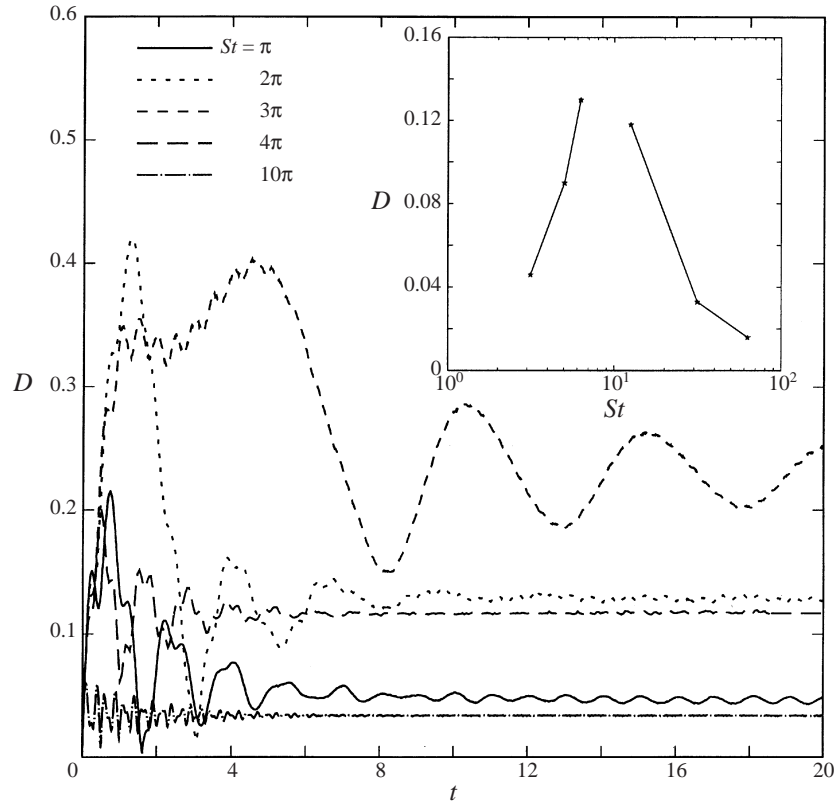
FIGURE 17. Effect of frequency on drop deformation in an RE flow at $Re = 10$ and $k = 200$. Inset shows long-time drop response for varying frequency.

frequencies, $St = 4\pi$, and 10π, D decreases. The long-time value of D with varying frequency is shown in the inset. Because of the slow decay near $St = 3\pi$, single long-time values were not obtained.

Figure 18 shows the resonance with changing interfacial tension for a fixed forcing frequency $St = 4\pi$. As with the case of fixed St, there is a gap near resonance, where long-time values are not available.

5.3. *Oscillatory extensional (OE) flow*

One could set up an oscillatory extensional flow in a four-roll mill. For a steady extensional flow the rolls are rotated at the same steady rotation, adjacent rolls in opposite directions. An oscillatory extensional flow (3.7) can be generated by varying the rotational rate in an identical time-periodic way for all the rolls.

The imposed flow again reduces to a steady extensional flow for $St = 0$. Our main interest here is to study the effects at non-zero St, more specifically the resonance phenomena that have been seen for the rotational flow in the above section. In figure 19 we show D as a function of time for varying frequency at $Re = 0.1$ and $k = 45$. Here, unlike the RE flow, D undergoes oscillations, reaching the undeformed value of zero. Note that the maximum value of D indeed first increases and then decreases with increasing frequency. Values of D_{max} are shown in figure 20 for $Re = 0.1$ and 1.0 at a fixed St and varying k, and fixed k and varying St along with corresponding curves of D from RE flows. It is shown that even though the flows
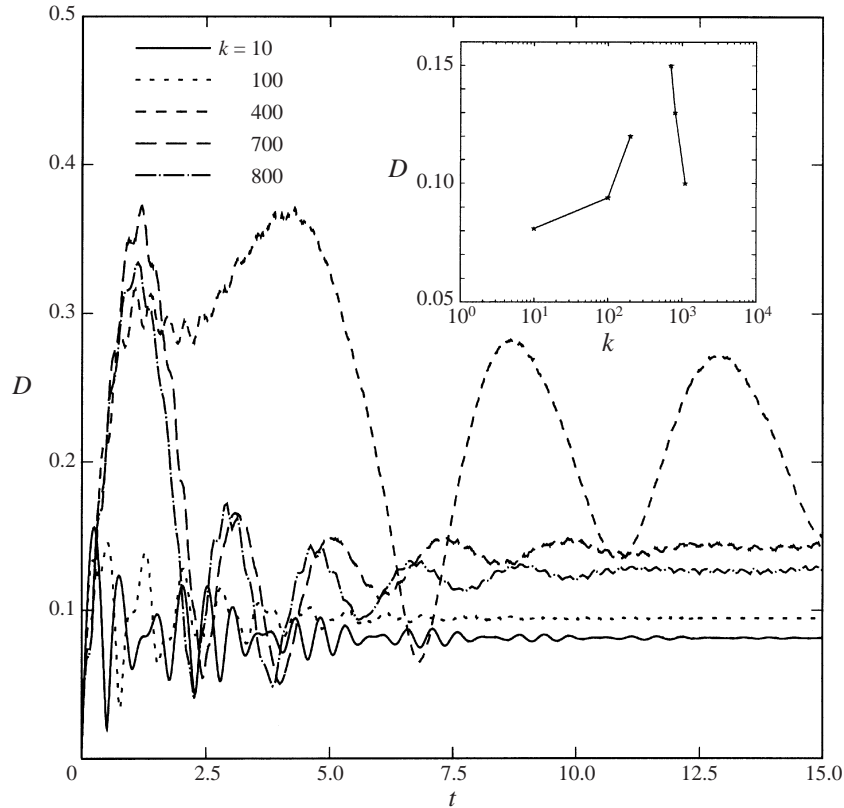
FIGURE 18. Effect of interfacial tension on drop deformation in an RE flow at $Re = 10$ and $St = 4\pi$. In the inset long-time drop response for varying tension is shown.

are very different in nature, the response in terms of long-time values of D_{max} shows surprising similarity as long as the defining characteristic St is kept the same. This further indicates the utility of the oscillator in explaining the essential physics of these flows.

6. Summary

We have numerically simulated the deformation of a two-dimensional drop in a potential vortex and other related flows at finite Reynolds numbers. An ADI front-tracking method was used. It incorporates modifications to earlier versions in order to extend the diffusion-dominated limits that have heretofore prevented applications to the low Reynolds numbers of interest here.

The velocity field due to the vortex has been modelled in the vicinity of the drop by a linear flow with time-periodic variation. The linearization introduces an error that is of higher order in a/R. This linearization will not be satisfactory if the drop undergoes continuing large deformation, such as would be the case if the interfacial tension were zero. In the cases reported here, linearization is believed to be a valid approximation.

The results show that in vortex-induced flow for low interfacial tension the drop experiences unbounded deformation. However above a critical value of k, the drop was found to reach a steady value of deformation even though the axes of deformation
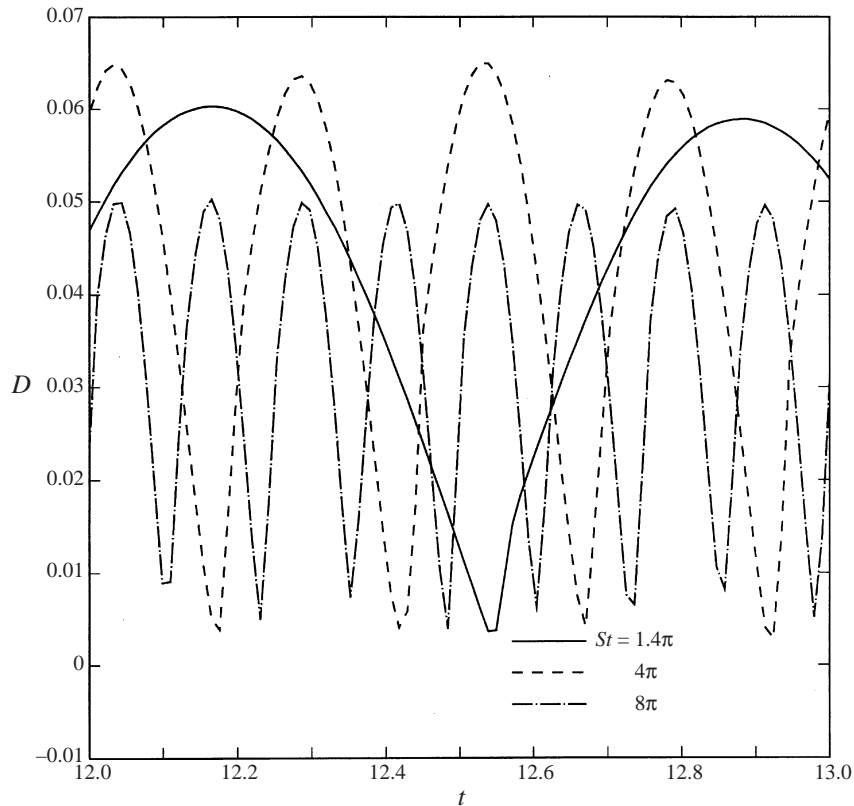
FIGURE 19. Effect of frequency on drop deformation in an OE flow at $Re = 0.1$ and $k = 45$.

revolve with the flow. Increased inertia leads to pronounced overshoot in deformation during the initial transient behaviour. With higher Reynolds number the deformation increases, and displays longer and more pronounced transients. Increased viscosity ratio leads to decreased deformation.

We also investigated drop deformation in a rotating extensional (RE) flow and an oscillatory extensional (OE) flow. The first is a generalization of the vortex-induced flow with the frequency of rotation varying independently of the shear rate. Therefore the behaviour is similar to that in a vortex, in that a drop reaches a steady value of deformation in the long-time limit.

In the zero frequency limit both of these flows reduce to steady extension. We have successfully compared the long-time equilibrium value of D in steady extension with those from the Stokes flow analysis performed by Buckmaster & Flaherty (1973). Finite inertia has significant effects on the transient and the long-time deformation of the drop. In contrast to a Stokes flow, the process of reaching an equilibrium shape in a steady flow is not monotonic, but the drop deformation overshoots before attaining the final state. For higher values of Reynolds number, the drop experiences an axis reversal, where the drop grows, collapses back to a circle, and then grows in an orthogonal direction. There are multiple growth–collapse cycles with or without axis reversal before the shape reaches a steady state.

In an RE flow, introduction of periodicity predictably leads to reduced deformation, which is the same response as that due to increasing the interfacial tension or the
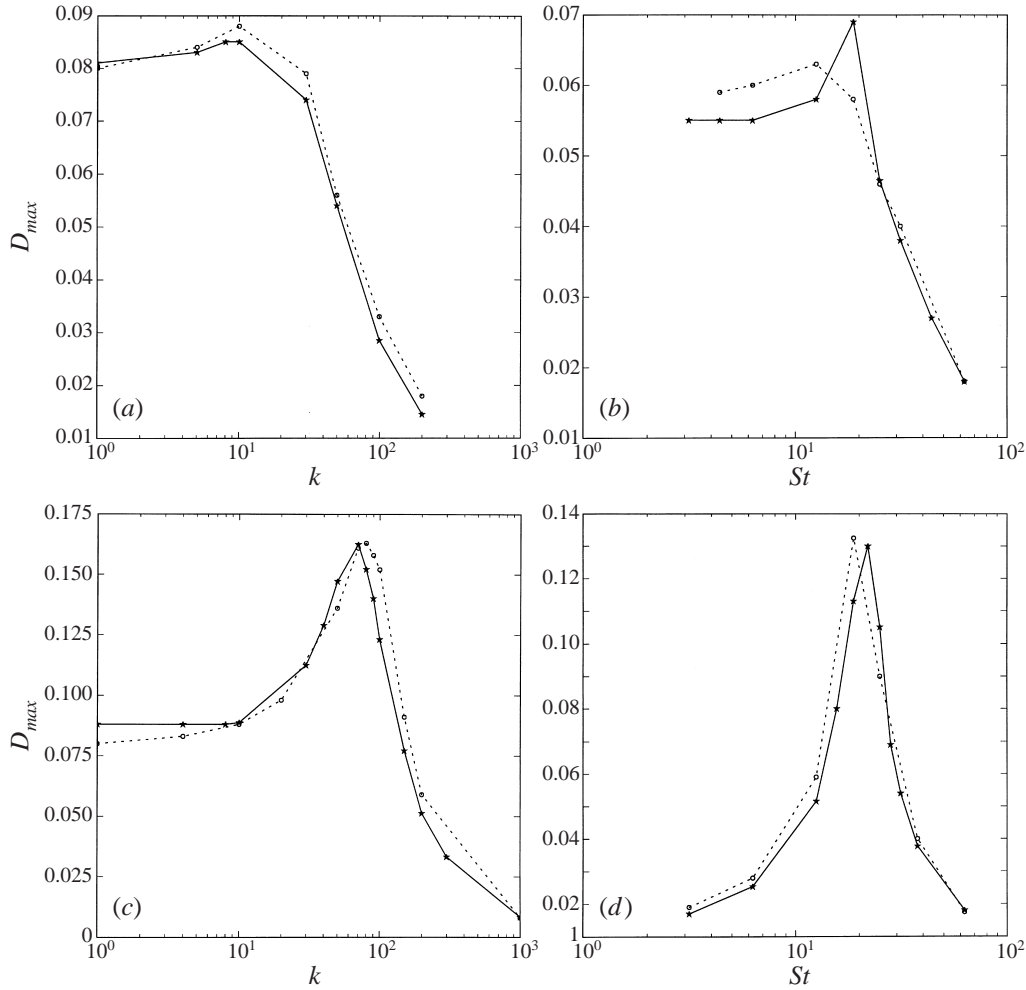
FIGURE 20. Long-time drop responses for RE (solid) and OE (dotted) flows for varying (*a*) interfacial tension at $Re = 0.1$, $St = 4\pi$; (*b*) frequency at $Re = 0.1$, $k = 45$; (*c*) interfacial tension at $Re = 1.0$, $St = 4\pi$; (*d*) frequency at $Re = 1.0$, $k = 200$.

viscosity ratio. A drop experiencing unbounded growth in a steady flow, reaches a bounded shape in an RE flow, when other parameters are unchanged. The drop shape in this state displays considerable interfacial-tension-dependent phase lag. The inverse power law decay in response observed with variation in frequency and interfacial tension is explained by the model presented in the Appendix. With increasing Reynolds number the initial transient is of course longer.

In both RE and OE flows, finite Reynolds number and periodic forcing introduce interesting physics to the problem. With increasing interfacial tension and forcing frequency, the long-time deformation value undergoes a resonance phenomenon, where deformation first increases, and then decreases. The behaviour is quantitatively similar in these two dissimilar flows. The effect is due to a resonance in the 'forced–damped mass–spring' system underlying the flow, interfacial tension and viscosity playing the role of the spring and the damper, respectively. Because of the lack of inertia ('mass'), an identical periodic simulation in the Stokes flow limit would not

display such resonance. The long-time behaviour, including the resonance, is dealt with analytically in a companion paper (Sarkar & Schowalter 2001). However a simple oscillator model, presented in the Appendix, elucidates the essential physics of the deformation process, including the resonance and large k/St scalings. Note that the model, for which the relevant non-dimensional parameters such as Re, k and St are defined, is not limited to two-dimensional flows, and therefore indicates that the present observations are also expected in three-dimensional simulations as well as in experiments.

Appendix

In a companion paper (Sarkar & Schowalter 2001) we have performed a perturbative analysis of the unsteady Stokes problem for drop deformation that captures the resonance characteristics shown in this paper. However the physical significance of different terms in the complex algebraic expressions can be difficult to identify. Here we have constructed a simple ODE model to describe the underlying physics of the drop deformation problem. Most of the salient features, including the different scaling observed in the numerical results, can be qualitatively explained by this model.

The deformation due to an external flow at a finite Reynolds number can be modelled as a damped mass–spring system with mass $\hat{\rho}\hat{a}^3$, damping $\hat{\mu}$, and interfacial tension $\hat{\sigma}$,

$$\hat{\rho}\hat{a}^3 \ddot{X} + \hat{\mu}\hat{a}\dot{X} + \hat{\sigma} X = \hat{\mu}\hat{a} G_0 g(t) + \hat{\rho}\hat{a}^3 G_0 \dot{g}(t), \quad \dot{X}(0) = G_0 g(0), \quad X(0) = 0, \quad \text{(A 1)}$$

where a hat has been used to differentiate the model variables from their real counterparts. The forcing terms in the right-hand side have been chosen to mimic the effect of the flow. The first forcing term corresponds to the viscous stress $\mu\dot{\gamma}$. The second term represents the pressure forcing. From the momentum equation, $\rho \partial u/\partial t \sim \nabla p$, one can see that a time-dependent velocity $G_0 g(t)$ will give rise to such a pressure (G_0 is the magnitude). The initial conditions reflect an undeformed drop moving with the imposed flow velocity. For a drop having density $\rho^* = \lambda_\rho \rho$, and viscosity $\mu^* = \lambda\mu$, different from that of the continuous phase, the mass and the damping terms in the above equations are modified by factors $(1+\lambda_\rho)/2$ and $(1+\lambda)/2$, respectively. Note these factors reduce to unity for identical material properties in two phases. By scaling length by $\hat{a}$ and time by $\hat{a}/G_0$ we obtain

$$\frac{(1+\lambda_\rho)}{2} \hat{Re} \ddot{X} + \frac{(1+\lambda)}{2} \dot{X} + \hat{k} X = g(t) + \hat{Re}\, \dot{g}(t), \quad \dot{X}(0) = g(0), \quad X(0) = 0, \quad \text{(A 2)}$$

where $\hat{Re} = \hat{\rho}\hat{a} G_0/\hat{\mu}$ and $\hat{k} = \hat{\sigma}/(\hat{\mu} G_0)$ are the Reynolds number and inverse capillary number of the model problem. Note that the pressure forcing is absent for Stokes flow ($\hat{Re} = 0$), and one obtains

$$\frac{(1+\lambda)}{2} \dot{X} + \hat{k} X = g(t), \quad X(0) = 0. \quad \text{(A 3)}$$

In that case for a constant external flow ($g(t) = 1$) the solution is

$$X = \hat{k}^{-1}(1 - e^{-2\hat{k}t/(1+\lambda)}), \tag{A 4}$$

which shows that $X\hat{k}$ is a function of $\hat{k}t/(1 + \lambda)$, and moreover $X \to \hat{k}^{-1}$ as $t \to \infty$. However for a time-periodic flow such as in the present work (vortex, RE, OE flows), $g(t) = \exp(i\hat{S}tt)$, one can see that time dependence of deformation $|X|$ is not just a simple function of $\hat{k}t$ (in the case of $\lambda = 1$) as has been noted in the section on vortex flow above. In fact the solution is

$$X = \frac{2e^{i\hat{S}tt}(1 - e^{-(\delta + i\hat{S}t)t})}{(1 + \lambda)i\hat{S}t + 2\hat{k}}, \quad \delta = \frac{2\hat{k}}{1 + \lambda}. \tag{A 5}$$

For non-zero Reynolds number, we look for a time-periodic solution $X = \tilde{X} \exp(i\hat{S}tt)$, and obtain (the long-time behaviour)

$$\tilde{X} = \frac{1 + i\hat{S}t\,\hat{Re}}{-\frac{1}{2}(1 + \lambda_\rho)\hat{S}t^2\hat{Re} + i\frac{1}{2}(1 + \lambda)\hat{S}t + \hat{k}}, \tag{A 6}$$

clearly showing the resonance characteristic of such systems, which disappears for $\hat{Re} = 0$. Equation (A 6) shows no direct scaling with $\hat{k}$. Even for Stokes flow $\tilde{X} = [i(1 + \lambda)\hat{S}t/2 + \hat{k}]^{-1}$ with no power law dependence on $\hat{k}$. However for $\hat{k} \to \infty$, we recover the asymptotic scaling $\tilde{X} \sim \hat{k}^{-1}$.

Keeping all other parameters constant, for $\hat{S}t \to \infty$ we obtain $\tilde{X} \sim \hat{S}t^{-1}$, for both zero and non-zero Reynolds number. This behaviour is amply demonstrated by the numerical solution. Note that the pressure forcing term $\sim \hat{S}t$ in the numerator is necessary to preserve the -1 power. Otherwise, for non-zero Reynolds numbers, the analysis would have erroneously predicted $\tilde{X} \sim \hat{S}t^{-2}$.

Some other interesting observations can be procured from expression (A 6) that are of value for interpreting the analytical results in Sarkar & Schowalter (2001). In the limit of $\hat{k} \to \infty$, the asymptotic expression $\sim \hat{k}^{-1}(1 + i\hat{S}t\hat{Re})$ is only a function of $\hat{S}t\hat{Re}$. For $\hat{S}t \to \infty$, the asymptotic expression $\sim [\hat{S}t(1 + \lambda_\rho)/2]^{-1}$ is only a function of λ_ρ. In the limit of $k \to 0$, for $\lambda = \lambda_\rho = 1$, the drop is passively advected, and therefore (A 6), that misleadingly indicates $\hat{Re}$ dependence, should be discounted. Instead, the limit is only a function of $\hat{S}t$, for in this limit of passive advection the Stokes solution itself is an exact solution of the full equation. On the other hand, the $\hat{S}t \to 0$ limit is independent of all variables except $\hat{k}$.

One other interesting limit is attained by letting $\hat{Re} \to \infty$. In this case the solution reaches a constant value, $\hat{S}t^{-1}(1 + \lambda_\rho)/2$. In fact in the companion paper the analytical solution matches this prediction. The present model is not expected to match the actual numerical value. However, in this particular case it so happens that the multiplying constant of proportionality turns out to be unity. Note again that absence of pressure forcing would have made the deformation vanish with $\hat{Re}^{-1}$. This limit is not the same as that of the inviscid potential flow, where due to vanishing viscosity $\hat{\mu}$, we also obtain $\hat{k} = \hat{\sigma}/(\hat{\mu}G_0) \to \infty$, but $\hat{k}' = \hat{k}/\hat{Re} = \hat{\sigma}/(\hat{\rho}\hat{a}G_0^2)$ reaches a constant value, and hence the equation becomes

$$\tfrac{1}{2}(1 + \lambda_\rho)\ddot{X} + \hat{k}'X = \dot{g}(t), \quad \dot{X}(0) = g(0), \quad X(0) = 0, \tag{A 7}$$

giving rise to a response

$$\tilde{X} = \frac{i\hat{S}t}{-\frac{1}{2}(1 + \lambda_\rho)\hat{S}t^2 + \hat{k}'},\qquad\text{(A 8)}$$

with resonance at $\hat{S}t = \sqrt{2\hat{k}'/(1 + \lambda_\rho)}$.

It is pertinent here to mention that a similar model ODE was studied by Kang & Leal (1990) in the context of bubble oscillation. Their model is derived from an asymptotic analysis for the critical Weber number in a steady inviscid straining flow (Kang & Leal 1988) coupled with Lamb's approximation of the damping term on the basis of dissipation (Lamb 1932, p. 640).

REFERENCES

ASTARITA, G. 1979 Objectivity and generally applicable criteria for flow classification. *J. Non-Newtonian Fluid Mech.* **6**, 69–76.

BENTLEY, B. J. & LEAL, L. G. 1986a A computer-controlled four-roll mill for investigations of particle and drop dynamics in a two-dimensional linear shear flow. *J. Fluid Mech.* **167**, 219–240.

BENTLEY, B. J. & LEAL, L. G. 1986b An experimental investigation of drop deformation and breakup in steady, two-dimensional linear flow. *J. Fluid Mech.* **167**, 241–283.

BLAKE, J. R. & GIBSON, D. C. 1987 Cavitation bubbles near boundaries. *Ann. Rev. Fluid Mech.* **19**, 99–123.

BUCKMASTER, J. D. & FLAHERTY, J. E. 1973 The bursting of two-dimensional drops in slow viscous flow. *J. Fluid Mech.* **60**, 625–639.

COX, R. G. 1969 The deformation of a drop in a general time-dependent fluid flow. *J. Fluid Mech.* **37**, 601–623.

DAVIES, J. T. & RIDEAL, E. K. 1963 *Interfacial Phenomena*. Academic.

DEIBER, J. A. & SCHOWALTER, W. R. 1992 The potential vortex as a prototype for predictions of polymer behaviour in unsteady and turbulent flows. *Proc. XIth Intl Cong. on Rheology, Belgium, August 17–21*, pp. 138–140. Elsevier.

EASTON, C. R. 1972 Homogeneous boundary conditions for pressure in the MAC method. *J. Comput. Phys.* **9**, 375–379.

ESMAEELI, A. & TRYGGVASON, G. 1998 Direct numerical simulations of bubbly flows. Part 1. Low Reynolds number arrays. *J. Fluid Mech.* **377**, 313–345.

ESMAEELI, A. & TRYGGVASON, G. 1999 Direct numerical simulations of bubbly flows. Part 2. Moderate Reynolds number arrays. *J. Fluid Mech.* **385**, 325–358.

FERZIGER, J. H. & PERIC, M. 1996 *Computational Methods for Fluid Dynamics*. Springer.

GODA, K. 1979 A multistep technique with implicit difference schemes for calculating two- or three-dimensional cavity flows. *J. Comput. Phys.* **30**, 76–95.

HOPFINGER, E. J., BROWAND, F. K. & GAGNE, Y. 1982 Turbulence and waves in a rotating tank. *J. Fluid Mech.* **125**, 505–534.

JACKSON, J. D. 1975 *Classical Electrodynamics*. John Wiley & Sons.

KANG, I. S. & LEAL, L. G. 1988 Small-amplitude perturbation of shape for a nearly spherical bubble in an inviscid straining flow (steady shapes and oscillatory motion). *J. Fluid Mech.* **187**, 231–266.

KANG, I. S. & LEAL, L. G. 1990 Bubble dynamics in time-periodic straining flows. *J. Fluid Mech.* **218**, 41–69.

KARNIADAKIS, G., ISRAELI, M. & ORSZAG, S. 1991 High-order splitting methods for the incompressible Navier–Stokes equations. *J. Comput. Phys.* **97**, 414–443.

KIM, J. & MOIN, P. 1985 Application of a fractional-step method to incompressible Navier–Stokes equations. *J. Comput. Phys.* **59**, 308–323.

LAMB, H. 1932 *Hydrodynamics*. Cambridge University Press.

MAXWORTHY, T., HOPFINGER, E. J. & REDEKOPP, L. G. 1985 Wave motions on vortex cores. *J. Fluid Mech.* **151**, 141–165.

Olbricht, W. L., Rallison, J. M. & Leal, L. G. 1982 Strong flow criteria based on microstructure deformation. *J. Non-Newtonian Fluid Mech.* **10**, 291–318.

Perot, J. B. 1993 An analysis of the fractional step method. *J. Comput. Phys.* **108**, 51–58.

Peskin, C. 1977 Numerical analysis of blood flow in the heart. *J. Comput. Phys.* **25**, 220–252.

Peyrot, R. & Taylor, M. 1986 *Computational Methods for Fluid Dynamics.* Springer.

Pozrikidis, C. 1992 *Boundary Integral and Singularity Methods for Linearized Viscous Flow.* Cambridge University Press.

Rallison, J. M. 1984 The deformation of small viscous drops and bubbles in shear flows. *Ann. Rev. Fluid Mech.* **16**, 45–66.

Sarkar K. & Schowalter, W. R. 2001 Deformation of a two-dimensional viscous drop in time-periodic extensional flows: analytical treatment. *J. Fluid Mech.* **436**, 207–230.

Seth, K. S. & Pozrikidis, C. 1995 Effects of inertia on the deformation of liquid drops in simple shear flow. *Intl J. Multiphase Flows* **26**, 65–102.

Stakgold, I. 1979 *Green's Function and Boundary Value Problems.* John Wiley & Sons.

Stone, H. A. 1994 Dynamics of drop deformation and breakup in viscous fluids. *Ann. Rev. Fluid Mech.* **26**, 65–102.

Sussman, M. & Smereka, P. 1997 Axisymmetric free boundary problems. *J. Fluid Mech.* **341**, 269–294.

Szeri, A. J., Wiggins, S. & Leal, G. 1991 On the dynamics of suspended microstructure in unsteady, spatially inhomogeneous, two-dimensional fluid flows. *J. Fluid Mech.* **228**, 207–241.

Tanner, R. I. 1976 A test particle approach to flow classification for viscoelastic fluids. *AIChE J.* **22**, 910–918.

Tanner, R. I. & Huilgol, R. R. 1975 On a classification scheme for flow fields. *Rheol. Acta* **14**, 959–962.

Taylor, G. I. 1932 The viscosity of a liquid containing small drops of another fluid. *Proc. R. Soc. Lond.* A **138**, 41–48.

Taylor, G. I. 1934 The formation of emulsions in definable fields of flow. *Proc. R. Soc. Lond.* A **146**, 501–523.

Taylor, G. I. 1964 Conical free surfaces and fluid interfaces. *Proc. 11th Intl Congr. Appl. Mech., Munich.*

Tryggvason, G., Bunner, B., Ebrat, O. & Taubar, W. 1998 Computation of multiphase flows by a finite difference front tracking method. I. Multi-fluid flows. *29th Computational Fluid Dynamics Lecture Series 1998-03. Von Karman Institute of Fluid Dynamics.*

Unverdi, S. O. & Tryggvason, G. 1988 A front-tracking method for viscous, incompressible multi-fluid flows. *J. Comput. Phys.* **100**, 25–37.